Spontaneous Surface Generation and Interior Amplification of Internal Waves in a Regional-Scale Ocean Model

CALLUM J. SHAKESPEARE AND ANDREW MCC. HOGG

Research School of Earth Sciences, and ARC Centre of Excellence in Climate System Science, Australian National University, Canberra, Australian Capital Territory, Australia

(Manuscript received 10 August 2016, in final form 15 December 2016)

ABSTRACT

Recent theories, models, and observations have suggested the presence of significant spontaneous internal wave generation at density fronts near the ocean surface. Spontaneous generation is the emission of waves by unbalanced, large Rossby number flows in the absence of direct forcing. Here, spontaneous generation is investigated in a zonally reentrant channel model using parameter values typical of the Southern Ocean. The model is carefully equilibrated to obtain a steady-state wave field for which a closed energy budget is formulated. There are two main results: First, waves are spontaneously generated at sharp fronts in the top 50 m of the model. The magnitude of the energy flux to the wave field at these fronts is comparable to that from other mechanisms of wave generation. Second, the surface-generated wave field is amplified in the model interior through interaction with horizontal density gradients within the main zonal current. The magnitude of the mean-to-wave conversion in the model interior is comparable to recent observational estimates and is the dominant source of wave energy in the model, exceeding the initial spontaneous generation. This second result suggests that internal amplification of the wave field may contribute to the ocean's internal wave energy budget at a rate commensurate with known generation mechanisms.

1. Introduction

Internal waves perform a vital role in the ocean energy cycle by exchanging energy with the mesoscale flow and ultimately breaking and driving mixing in the deep ocean (Wunsch and Ferrari 2004). The classical picture of the ocean wave field has sources of wave energy at ocean boundaries due to barotropic tides washing over rough bottom topography and high-frequency surface wind stresses (Munk 1981). More recently, it has been shown that geostrophic eddies interacting with rough bottom topography can generate significant internal lee waves (Nikurashin and Ferrari 2011). Surface wave generation is also anticipated due to ''forced imbalances'' (such as from surface buoyancy fluxes), which can drive geostrophic adjustment (e.g., Blumen 1972) or dynamical instabilities, which then generate waves as they evolve (e.g., Plougonven and Zeitlin 2009; Ribstein et al. 2014; Grisouard et al. 2016). Nagai et al. (2015) and Shakespeare and Taylor (2016), among others, have further argued that there can be significant spontaneous wave generation in regions of highly unbalanced flow near the ocean surface. Lee waves generated from geostrophic flow and spontaneous generation both transfer energy from the mesoscale flow to the wave field and are thus potentially important both as sources for the global internal wave field and as sinks of mesoscale energy. Nikurashin and Ferrari (2011) have quantified the wave energy source associated with lee waves generated from geostrophic flow as 0.2 TW, similar to the estimated energy input to the wave field due to high-frequency winds. The spontaneous generation of internal waves near the ocean surface has not yet been quantified.

Spontaneous generation occurs in regions of highly unbalanced flow near the ocean surface, characterized by order one Rossby numbers (Ro). Modeling studies (e.g., Danioux et al. 2012) indicate that much of this generation occurs at sharp density fronts and filaments when they are being actively strained, sheared, or otherwise sharpened—a process known as frontogenesis. Shakespeare and Taylor (2016) and Lott et al. (2010) have presented linear theories for the spontaneous generation of waves as a result of the horizontal straining and vertical shearing of potential vorticity anomalies (fronts). While these theories demonstrate the potential

Corresponding author e-mail: Callum J. Shakespeare, callum.shakespeare@anu.edu.au

DOI: 10.1175/JPO-D-16-0188.1

for an energy transfer from the larger-scale flow to the wave field (Shakespeare 2015), the linear nature and approximations implicit in these theories prevent definitive estimates of the net wave energy flux for realistic ocean fronts. An alternative approach is to quantify the spontaneous generation directly from an idealized numerical model, such as the Nagai et al. (2015) study of the Kuroshio Current. Crucial to this analysis is a rigorous definition of the wave field in the numerical model, thereby allowing quantification of the energy flux into the wave field. An internal wave may be defined as a motion of Lagrangian frequency (i.e., the frequency following the local flow) exceeding the inertial frequency (Polzin and Lvov 2011). This Lagrangian definition of internal waves addresses the issue of significant Doppler shifting of the wave frequency by the nonwave flow, which is common in regions of spontaneous generation (e.g., Shakespeare and Taylor 2016). To our knowledge, Nagai et al. (2015) are the first to directly apply such a Lagrangian filter to the output fields of a large-scale numerical model to determine the internal wave and nonwave constituents. A similar approach is taken in the present work.

Explicit expressions for the internal energy fluxes to and from the wave field may be determined by (Lagrangian) filtering the momentum and buoyancy equations to form a wave energy equation (e.g., Muller 1976; Polzin 2010). In the absence of boundary forcing, the only possible sources of wave energy are mean-to-wave conversions within the flow. However, the presence of a positive mean-to-wave conversion does not necessarily imply local spontaneous generation, since these terms also describe the amplification of a preexisting wave field (e.g., Whitt and Thomas 2015). Furthermore, Thomas (2012) describes how internal waves can both extract energy from and transfer energy to the nonwave flow, in the presence of frontogenetic strain and vertical shear, even in a highly idealized flow. Spontaneous generation is only likely to be active when there is highly unbalanced flow and strong frontogenesis coincident with large, positive, mean-to-wave energy fluxes (e.g., Nagai et al. 2015), although a rigorous separation of spontaneous generation versus secondary amplification is not possible. Spontaneously generated waves may be reabsorbed by the mean flow; for example, when they approach a critical layer (Booker and Bretherton 1967). In their Kuroshio model, Nagai et al. (2015) report $O(10)\,\mathrm{mW\,m^{-2}}$ spontaneous wave generation, with 85% of this being reabsorbed by the mean flow near the surface. These studies suggest that waves continually transfer energy to and from nonwave flows and thereby play a rather complex role in the ocean's energy budget, something that will be further investigated in the present work.

In this paper, we configure a model to examine the rate of spontaneous generation of internal waves in an idealized domain with a Southern Ocean–like parameter regime. Our model differs from that of Nagai et al. (2015) in several ways. The most significant difference is that we examine a model in a statistical steady state rather than a spindown simulation of a current, as in Nagai et al. (2015). Furthermore, we have a larger domain (500-km square) at higher resolution (200 m rather than 500 m), permitting a better representation of smaller-scale internal waves. We use lower explicit viscosity and diffusivity, with parameters chosen to minimize the spurious decay of resolved waves while maintaining model stability (Shakespeare and Hogg 2017). Our analysis methodology also differs. We find it necessary to modify the classical internal wave energy budget (Muller 1976), which assumes a quasigeostrophic (QG) large-scale flow, to account for generation from non-QG surface flows and associated wave–mean temporal correlations. This modification permits us to fully close the wave energy budget in our model and to quantify the magnitude and spatial locations of individual sources and sinks of wave energy. Intriguingly, this analysis reveals that the model interior is a very significant source of wave energy, with waves drawing from the available potential energy of finescale buoyancy gradients. To our knowledge, this behavior has not been previously observed in a numerical model, but similar results have been obtained from analysis of mooring data from the Gulf Stream recirculation region (Polzin 2010).

The paper is set out as follows: In section 2, we introduce the numerical model configuration and describe the filtering of the model fields into wave and nonwave parts (section 2a). We close the wave energy budget for the model in section 3 and identify four depth bands that correspond to distinct sources and sinks of wave energy. The behavior of internal waves in each layer is then described in detail. Last, in section 4, we discuss the significance of our results in quantifying sources and sinks of wave energy in the global ocean.

2. Methods

We use the Massachusetts Institute of Technology Global Circulation Model (MITgcm; Marshall et al. 1997) to simulate the hydrostatic primitive equations in a 500-km-square, 3.7-km-deep, zonally reentrant, flat-bottomed, *f*-plane channel at 200-m horizontal resolution. The vertical grid consists of 200 points with grid spacing of 1.5 m at the surface; increasing to 40 m at middepth and reducing to 20 m in the deepest 1 km of the domain (see Fig. 1a). The model is forced by "sponges" of 30-km width just inside the northern and southern boundaries where densities (temperatures; salinity is constant) are restored to specified profiles (shown in Fig. 1b, chosen to approximate the parameter

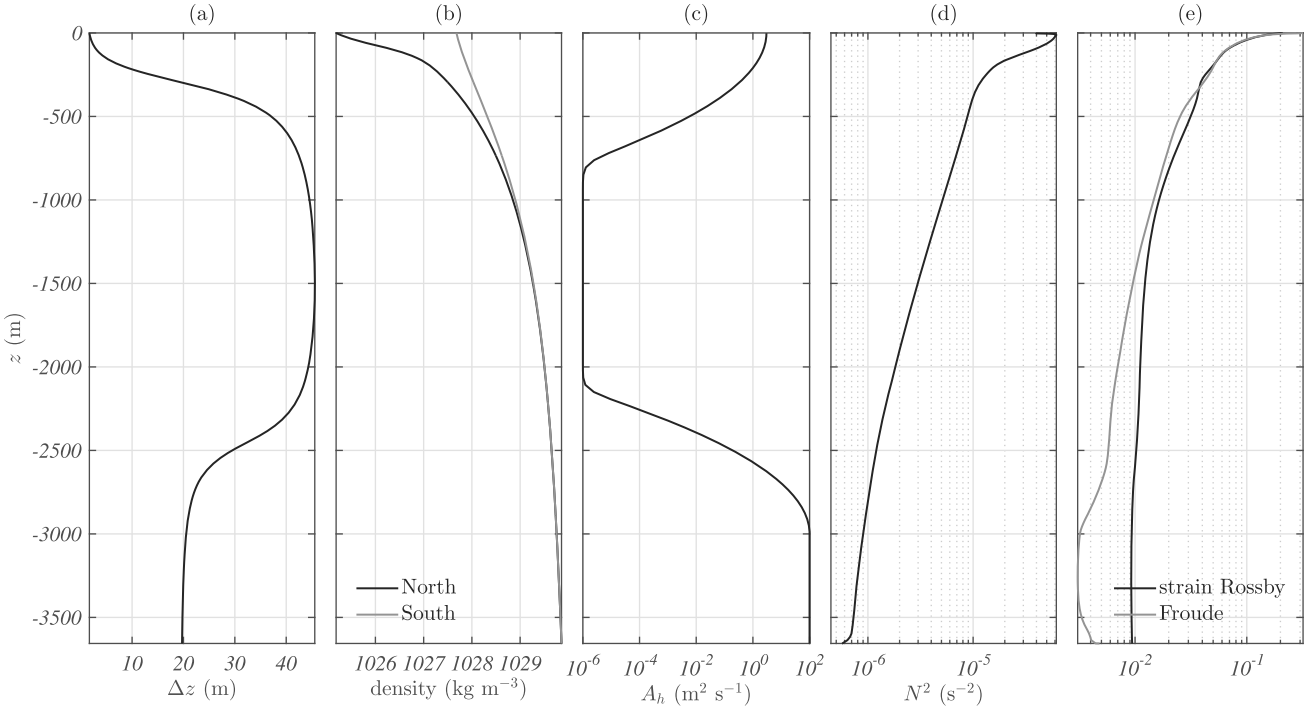

FIG. 1. Configuration of the numerical model. (a) Vertical resolution. (b) Density profiles to which the model is restored at the north (black) and south (gray) boundaries on a 10-day time scale. (c) The horizontal Laplacian viscosity. (d) Time- and space-averaged stratification N^2 in the model at steady state. (e) The time- and space-averaged strain Rossby number $\mathrm{Ro} = f^{-1}\sqrt{(\partial u/\partial x)^2 + (\partial u/\partial y)^2 + (\partial v/\partial x)^2 + (\partial v/\partial y)^2}$ (black) and Froude number $\mathrm{Fr} = N^{-1}\sqrt{(\partial u/\partial z)^2 + (\partial v/\partial z)^2}$ (gray) at steady state.

regime of the Southern Ocean) on a 10-day time scale. The restoring period and spatial extent of the sponges are chosen such that the sponge will not affect the wave field (see the appendix). There is no surface buoyancy flux or wind stress. A quadratic bottom drag with dimensionless coefficient $C_d = 1 \times 10^{-3}$ is applied. Subgrid turbulence is parameterized via Laplacian diffusion and viscosity. However, our turbulent parameter choices are not intended to be a realistic representation of subgrid processes and are chosen purely to minimize their effect on the resolved wave field while maintaining numerical stability (Shakespeare and Hogg 2017). To this end, we use a horizontal viscosity of $A_h = 3\,\mathrm{m^2\,s^{-1}}$ (shown in Fig. 1c) near the surface to prevent the collapse of flow gradients below the grid scale. This viscosity decays in a Gaussian fashion over the top 200 m to a negligible interior value ($10^{-6}\,\mathrm{m^2\,s^{-1}}$) so that any effect on the wave field will be localized to the surface region. Guided by the results of Shakespeare and Hogg (2017), in order to maintain stability in the model interior with negligible spurious wave decay, we apply a uniform horizontal diffusivity of $\kappa_h = 0.1\,\mathrm{m^2\,s^{-1}}$ (constant over the entire domain). In the absence of boundary fluxes there is no requirement for significant vertical viscosity or diffusivity, and these parameters are set to a negligible value everywhere ($A_v = \kappa_v = 10^{-6}\,\mathrm{m^2\,s^{-1}}$). Last, we employ a viscous sponge ($A_h = 100\,\mathrm{m^2\,s^{-1}}$) in the bottom 900 m of the domain to absorb downward-propagating waves and minimize reflection of waves off the flat bottom.

The 200-m-resolution model is initialized from a 500-m-resolution model with a fully equilibrated mesoscale eddy field. The 200-m-resolution model is run for 2 months to permit the submesoscale and wave fields to equilibrate, after which we output 1 week of model data at hourly time intervals and analyze the internal wave field. This relatively long spinup procedure ensures that the wave field does not contain signals from adjustment or equilibration processes. Furthermore, the absence of topography and surface forcing means that there is no external forcing of the wave field and thus all waves observed have been generated spontaneously by the flow. The temporal and horizontally averaged stratification in the model at steady state is shown in Fig. 1d, and the Rossby and Froude numbers are shown in Fig. 1e (see caption for definitions). At the surface the mean strain Rossby number is 0.21 and the mean Froude number is 0.32, implying an active submesoscale is present.

a. Defining internal waves in the numerical model

Before analyzing the model output, we must specify exactly how the wave field is defined. Theoretically,

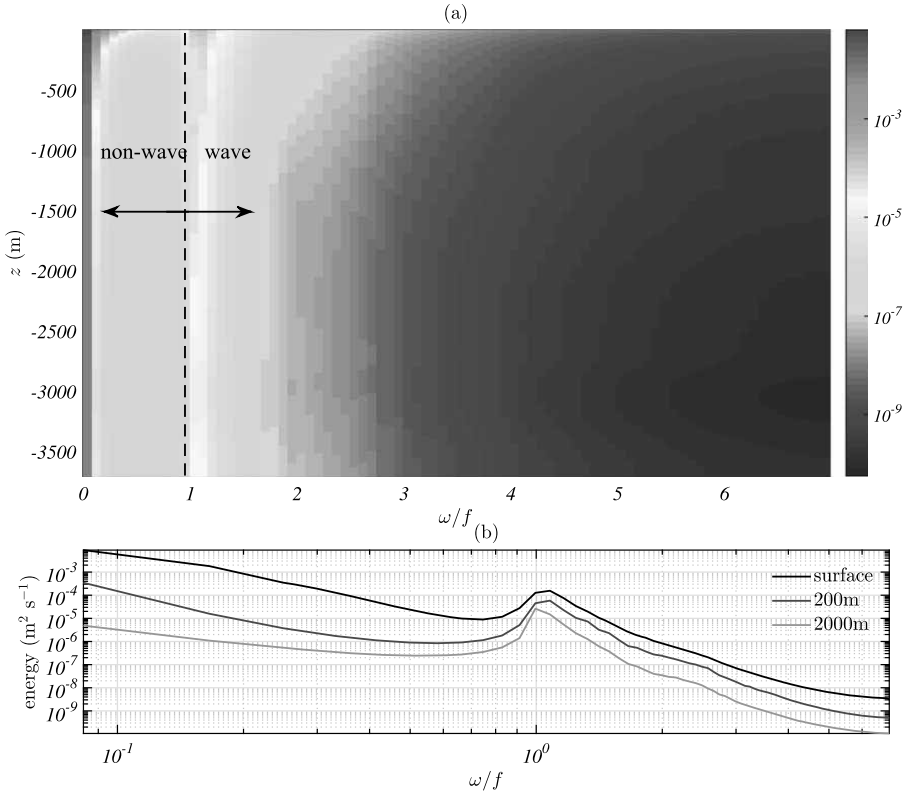

FIG. 2. The kinetic energy spectrum ($m^2\,s^{-1}$) averaged along particle trajectories as a function of Lagrangian frequency ω (normalized by f) and depth z. (a) Contour plot over all depths with the cutoff frequency for the high-pass filter is indicated by a dashed line. (b) Log–log plot for three individual depths (see legend).

hydrostatic internal waves may be defined as motions with Lagrangian frequencies—that is, the frequency measured in a coordinate following the flow—exceeding $|f|$ (Polzin and Lvov 2011). This definition accounts for the Doppler shifting associated with stationary and trapped waves, which are common near the ocean surface. To apply this definition in our model, we initialize a flow-following particle at every model grid point (1.4 billion particles in total) at the start of the 1-week analysis period and compute the particle trajectory over this week. Similar to Nagai et al. (2015), here we use a "semi-Lagrangian" approach where we follow the flow in the horizontal direction only. The semi-Lagrangian approach does not account for Doppler shifting due to the vertical velocity, but this effect is not expected to be particularly significant.[1]

The (Eulerian) model fields are interpolated to the particle trajectories to yield Lagrangian fields. Fourier transforming the Lagrangian fields in time yields the Lagrangian frequency spectrum.

Figure 2 shows the frequency spectrum for particle-averaged kinetic energy as a function of depth. For 1 week of hourly data the maximum frequency resolvable is $\pi/(1\text{ hour}) = 6.9f$, and the frequency resolution is $\pi/(1\text{ week}) = 0.04f$. Even near the surface (where submesoscales are present) there is a clear time-scale separation between nonwave energy concentrated at frequencies less than $0.5f$ and wave energy at frequencies greater than or equal to f. The wave field is obtained by applying a high-pass filter with a sharp cutoff at $0.9f$ (indicated by the dashed vertical line in Fig. 2a) to ensure that the inertial peak in the spectrum is fully included in the wave field. The high-pass filtering inevitably causes ringing at the beginning and end of the 1-week period. To avoid this effect we truncate the first and last 36 h and use only the middle 4 days of filtered data in our analysis and space–time averaging. The final step is to interpolate the filtered (wave) field defined along particle paths back to the original model grid at each time to yield the wave field

[1] To estimate the error, note that (from classical ray tracing theory) the Doppler shift due to a uniform velocity W for a wavenumber m in the same direction is $\Delta\omega = mW$. If we consider the extreme case of a submesoscale front with a depth-averaged (over the top 200 m) vertical velocity of $50\,m\,day^{-1}$ acting on a wave with $m = 2\pi/200\,m^{-1}$, the error in Lagrangian frequency would be $0.14f$. For comparison, the horizontal Doppler shift due to a front with horizontal velocity $U = 0.05\,m\,s^{-1}$ and $k = 2\pi/2000\,m^{-1}$ is $\Delta\omega = Uk = 1.25f$.

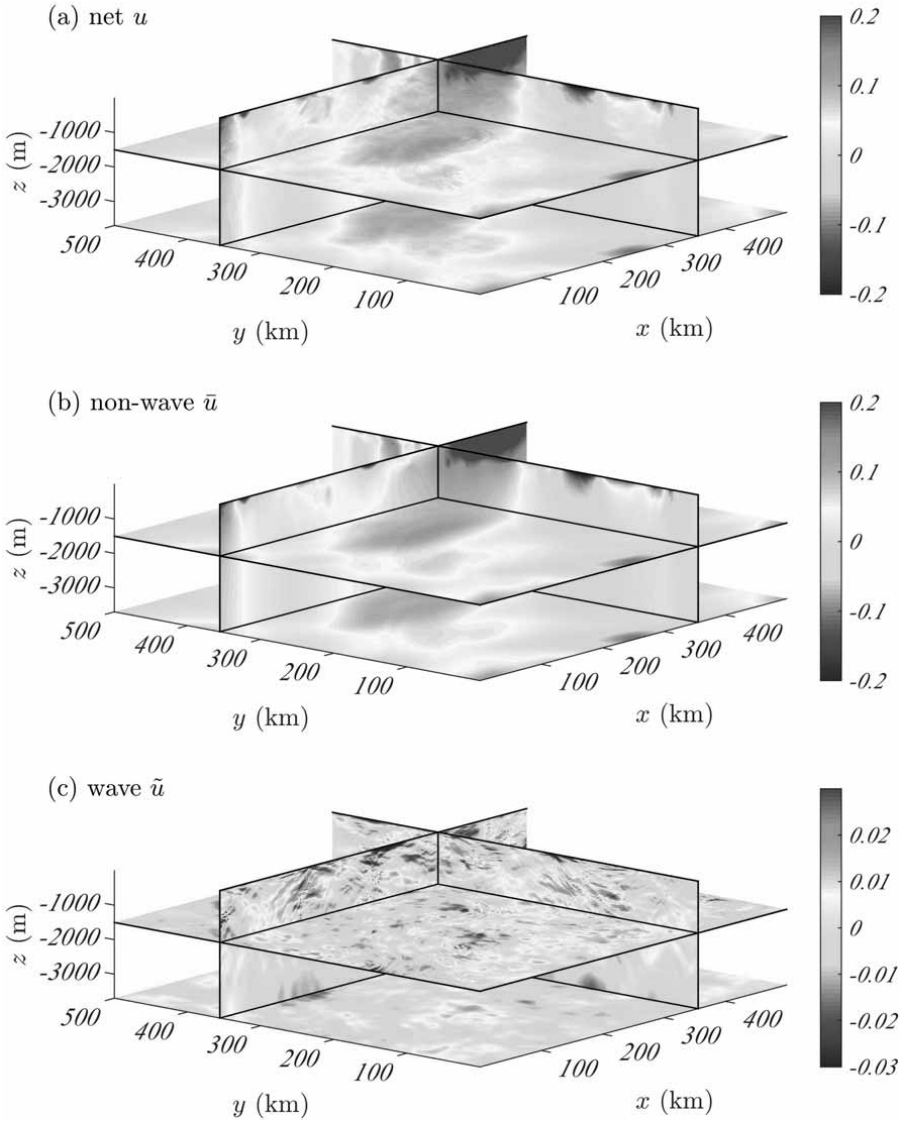

FIG. 3. The zonal velocity ($m\,s^{-1}$) from the model at an instant in time. (a) The net zonal velocity u. (b) The nonwave zonal velocity $\overline{u}$. (c) The wave zonal velocity $\tilde{u}$; the difference between (a) and (b).

defined in Eulerian space, denoted by a tilde $\tilde{\eta}$ (where η is a dummy variable representing any field of interest). The ''nonwave'' or mean field, denoted by a bar $\overline{\eta}$, is the difference between the original unfiltered field and the wave field, $\overline{\eta} = \eta - \tilde{\eta}$ (both described in Eulerian space). We note that the mean field defined in this manner is time dependent and is entirely different from the long-term, temporal-averaged ''mean'' defined in eddy–mean frameworks. The above filtering procedure is applied to the pressure and the three velocity components (u, v, w) independently. The wave buoyancy is then computed assuming hydrostatic balance: $\tilde{b} = \partial_z \tilde{p}/\rho_0$.

Figure 3 shows a snapshot of the model zonal velocity filtered into its wave and nonwave components as described above. Wave horizontal flow speeds are typically 1 to 3 $cm\,s^{-1}$ or about 10% of mean flow speeds. Waves exist in the model over all horizontal scales but with peak wave kinetic energy (relative to the nonwave flow) at wavelengths between 5 and 20 km.

b. *Wave energy budget*

In the appendix, we derive a generic wave energy budget for a hydrostatic, flat-bottomed numerical model. Unlike previous wave energy equations (Muller 1976) we make no assumption as to the quasigeostrophy of the nonwave flow fields. The resultant wave energy budget possesses analogous terms to the Muller (1976) equations (see also Polzin 2010; Nagai et al. 2015) but with different space and time averaging. Here, we use

angled brackets to denote horizontal space and time averaging:

$$\langle \eta \rangle = \frac{\int_0^T \iint \eta \, dx \, dy \, dt}{\int_0^T \iint 1 \, dx \, dy \, dt}, \tag{1}$$

where η is again a dummy variable. The only assumption required in the derivation of the energy budget is that there exists a spatiotemporal-scale separation between the wave and nonwave fields (which we have already shown to approximately hold; e.g., Fig. 2) such that the spatiotemporal average of the product of any wave field $\tilde{\eta}$ and any nonwave field $\overline{\theta}$ is zero: $\langle \tilde{\eta}\overline{\theta} \rangle = 0$. The details of the derivation are in the appendix; here, we will merely define the relevant energy reservoirs and significant energy sources and sinks in our model. The wave kinetic energy is defined as

$$\tilde{K} = \left\langle \frac{1}{2}(\tilde{u}^2 + \tilde{v}^2) \right\rangle, \tag{2}$$

and consistent with Polzin (2010), we define the wave available potential energy (APE) as

$$\tilde{A} = \left\langle \frac{\tilde{b}^2}{2N^2} \right\rangle, \tag{3}$$

where $N^2 = \partial_z \langle \overline{b} \rangle$ is the mean stratification at depth z.[2] The sign-definite energy sinks are the interior viscous dissipation of wave kinetic energy

$$\tilde{\varepsilon} = \left\langle A_h |\nabla_h \tilde{\mathbf{u}}_h|^2 + A_v \left| \frac{\partial \tilde{\mathbf{u}}_h}{\partial z} \right|^2 \right\rangle, \tag{4}$$

the irreversible mixing of density by waves

$$\tilde{\phi}_i = \left\langle \frac{\kappa_h}{N^2} |\nabla_h \tilde{b}|^2 + \frac{\kappa_v}{N^2} \left(\frac{\partial \tilde{b}}{\partial z} \right)^2 \right\rangle, \tag{5}$$

and the quadratic bottom drag on the wave field

$$\tilde{D} = \int_{\text{bot}} \tilde{\mathbf{u}}_h \cdot \tilde{\boldsymbol{\tau}}_h \, dS, \tag{6}$$

where $\tilde{\boldsymbol{\tau}}_h = C_d \sqrt{u^2 + v^2} \tilde{\mathbf{u}}_h$ is the parameterized stress (due to the wave field) in the bottom layer of the model. In the absence of boundary wave sources such as wind stresses or flow–topography interactions, as in the present model, the only other significant energy exchanges are mean-to-wave (MTW) interactions:

$$\begin{aligned} \text{MTW} = & \underbrace{\left\langle -\tilde{w}\tilde{\mathbf{u}}_h \cdot \frac{\partial \overline{\mathbf{u}}_h}{\partial z} \right\rangle}_{\text{vert. shear}} + \underbrace{\left\langle -\tilde{b}\tilde{\mathbf{u}}_h \cdot \frac{\nabla_h \overline{b}}{N^2} \right\rangle}_{\text{potential}} \\ & + \underbrace{\left\langle -\tilde{u}^2 \frac{\partial \overline{u}}{\partial x} - \tilde{v}^2 \frac{\partial \overline{v}}{\partial y} \right\rangle}_{\text{strain}} + \underbrace{\left\langle -\tilde{u}\tilde{v} \left(\frac{\partial \overline{u}}{\partial y} + \frac{\partial \overline{v}}{\partial x} \right) \right\rangle}_{\text{hz. shear}}. \end{aligned} \tag{7}$$

The sign convention adopted here is that a positive value of MTW is a transfer from the mean to the wave field. The vertical shear term describes a transfer of mean kinetic energy to wave kinetic energy through the mean vertical shear. The potential term describes a transfer of mean APE associated with horizontal buoyancy gradients (fronts) to wave APE. The vertical shear and potential terms are closely related when the mean flow is geostrophic. The strain term describes the transfer of mean kinetic energy to wave kinetic energy in a confluent mean flow (and is the energy source term that appears in the theory of spontaneous generation at strained fronts; see Shakespeare 2015). The horizontal shear term describes the transfer of mean kinetic energy to wave kinetic energy associated with horizontal mean shear (i.e., cross derivatives).

The above definition of the mean-to-wave interaction terms [Eq. (7)] differs from previous implementations [e.g., Nagai et al. 2015, their Eq. (2)] in that the time averaging is carried out after the multiplication of the mean and wave terms. Our approach accounts for temporal correlations of mean flow gradients and anomalously large wave amplitudes. Such correlations are expected to result from spontaneous generation events where, for example, large wave amplitudes will occur at the same time as large mean flow strain rates (e.g., Shakespeare and Taylor 2016). Tests using our model output (not shown) indicate that ignoring these temporal correlations leads to a consistent underestimate of the mean-to-wave terms by up to 50% near the surface.

3. Results

The time- and space-averaged interior wave energy sources and sinks identified in Eqs. (4)–(7) are shown in Fig. 4 as a function of depth. First, consider the sign-definite wave energy sinks: irreversible mixing (dotted–dashed blue) and viscous dissipation (dashed blue). The irreversible mixing by waves is substantial near the surface ($\sim 10^{-9}\,\text{W kg}^{-1}$) and decays smoothly with depth

[2] The APE defined by Eq. (3) is not the exact Winters et al. (1995) APE but is a good approximation for internal waves in the present model.

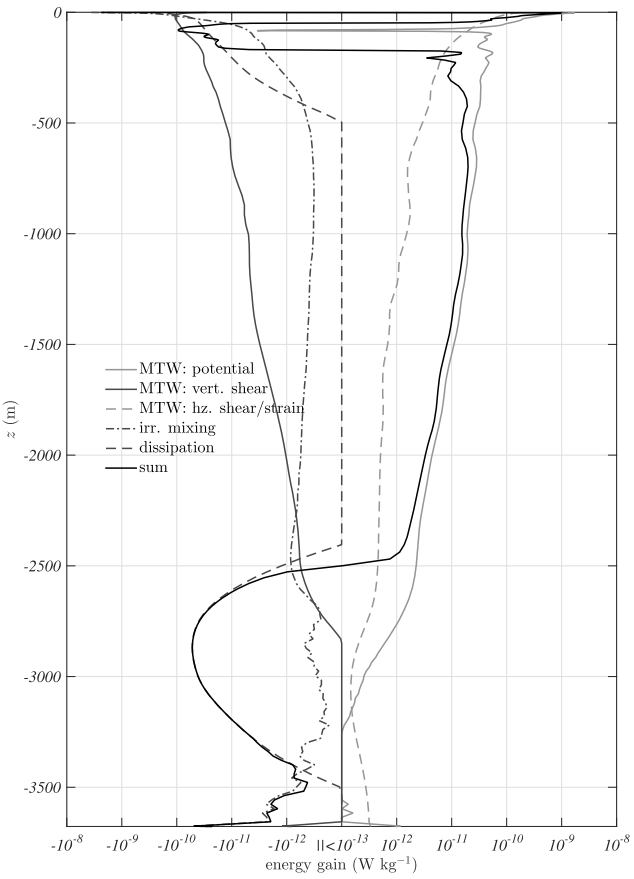

FIG. 4. Time- and space-averaged sources (red) and sinks (blue) of wave energy as a function of depth, and the total gain (black) in wave energy at each depth. The double-sided log scale only displays amplitudes exceeding $10^{-13}\,\mathrm{W\,kg^{-1}}$. There is a net source of wave energy above 50 m and between 175- and 2500-m depth. There is a net sink of wave energy between 50 and 175 m (the thermocline) and below 2500 m (in the sponge region).

(the diffusivity is a constant). As might be anticipated, the viscous dissipation is large near the surface (where the viscosity is amplified) and also in the viscous sponge below 2500 m. The dissipation peaks at 2800 m where the sponge viscosity first reaches its maximum value of $100\,\mathrm{m^2\,s^{-1}}$ (see Fig. 1); as the waves dissipate within the sponge, there is subsequently less wave energy at greater depths and thus the dissipation decreases. Now consider the mean-to-wave terms defined as per Eq. (7). The mean-to-wave potential term (solid red) is the largest-amplitude, mean-to-wave term and is positive everywhere except a narrow band around 100-m depth. The mean-to-wave horizontal shear and strain terms are both positive at all depths and have similar vertical structure and amplitude, and therefore only their sum is shown (dashed red). The mean-to-wave vertical shear term (solid blue) is negative at all depths, and away from the surface tends to partially counteract the potential term.

The sum of the five interior source and sink terms is shown in black and indicates four distinct source and sink layers. The surface layer, above 50-m depth, is a net source of wave energy, dominated by the mean-to-wave potential term, with mean-to-wave strain and horizontal shear also providing significant contributions. This region is characterized by high Rossby number (unbalanced) flows and is where spontaneous generation is expected to take place. The second ''thermocline'' layer between 50- and 175-m depth is a net sink of wave energy, primarily through viscous dissipation. The third layer between 175- and 2500-m depth corresponds to the ocean interior. In the interior layer the energy balance is dominated by the mean-to-wave potential term, which provides a net source of wave energy exceeding $10^{-11}\,\mathrm{W\,kg^{-1}}$ down to 1000-m depth. We show below that this interior input to the wave field is not spontaneous generation (since the flow is essentially geostrophic) but instead describes the energization of downward-propagating, surface-generated waves. The fourth and final layer below 2500-m depth corresponds to the viscous sponge and is dominated by the viscous dissipation of wave energy.

The energetics of the wave field in the surface, thermocline, and interior regions is considered in more detail in the following sections.

a. Surface layer

Figures 5a–c displays snapshots of the surface flow. The flow is highly unbalanced with the Rossby number (Fig. 5a) exceeding 1, particularly along elongated filaments (density fronts) and in some submesoscale eddies. The flow is dominated by a main zonal current through the center of the channel, indicated by the band of elevated mean kinetic energy (Fig. 5b). The region to the south of this zonal current (which has weaker stratification than to the north) is characterized by a network of sharp fronts and filaments (Fig. 5c) in between meso- and submesoscale eddies. Spontaneous generation of waves is anticipated at fronts undergoing rapid sharpening or ''frontogenesis'' (e.g., Shakespeare and Taylor 2014). Frontogenesis can be quantified by the frontogenesis function (Miller 1948), defined as the rate of increase in horizontal mean buoyancy gradient magnitude following the fluid motion due to adiabatic effects only (i.e., not including diffusion):

$$\frac{D|\nabla_h \overline{b}|}{Dt} = \underbrace{-\frac{(\nabla_h \overline{b}\cdot\nabla_h \overline{\mathbf{u}})\cdot\nabla\overline{b}}{|\nabla_h \overline{b}|}}_{\text{mean}} \underbrace{-\frac{(\nabla_h \overline{b}\cdot\nabla_h \tilde{\mathbf{u}})\cdot\nabla\overline{b}}{|\nabla_h \overline{b}|}}_{\text{wave}}, \qquad (8)$$

split here into mean-forced and wave-forced components. A positive value indicates sharpening of frontal

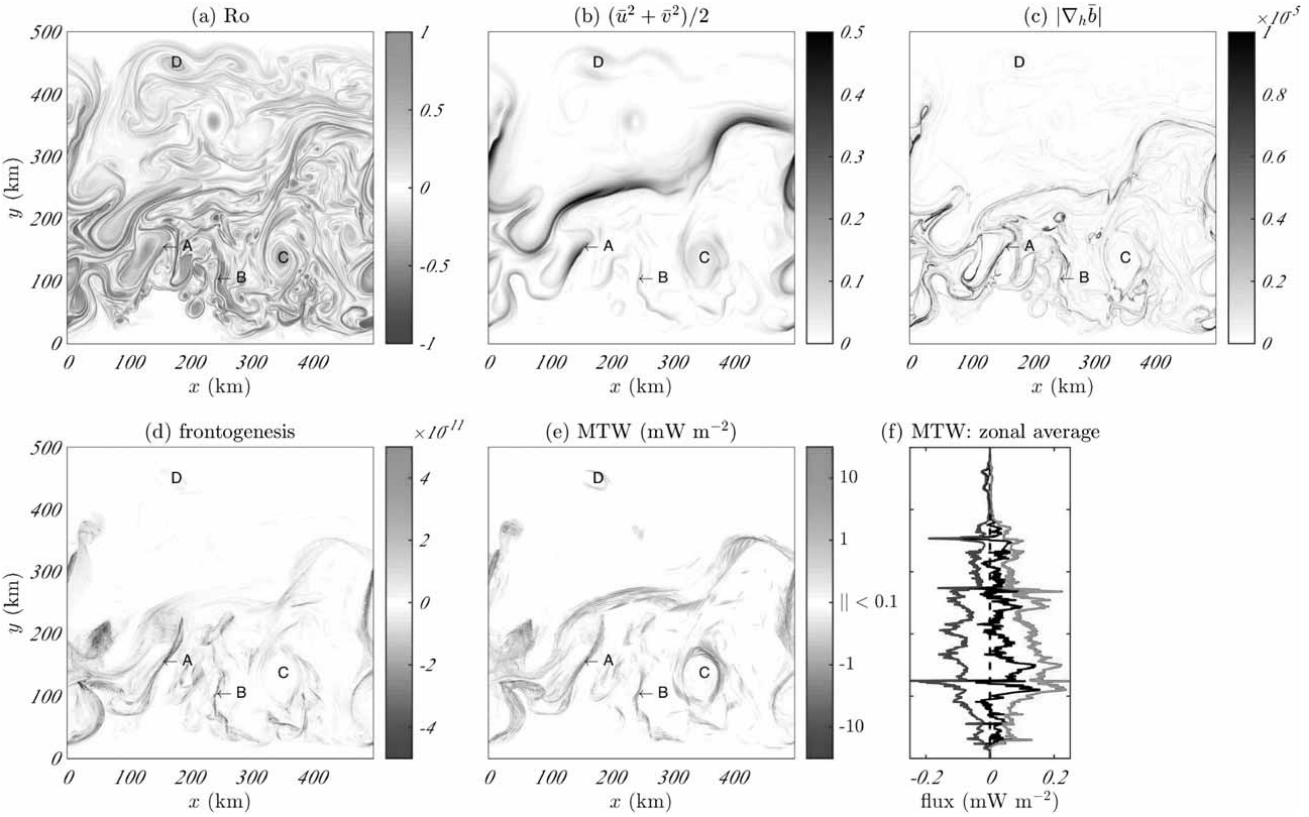

FIG. 5. Surface layer. Snapshot of (a) the vorticity Rossby number Ro = $(\partial_x \bar{v} - \partial_y \bar{u})/f$, the mean kinetic energy $(\bar{u}^2 + \bar{v}^2)/2$ (m^2 s^{-2}) and, (c) the horizontal buoyancy gradient magnitude $|\nabla_h \bar{b}|$ (s^{-2}). (d) Time-averaged mean frontogenesis function [Eq. (8); s^{-3}]. (e) The depth-integrated and time-averaged MTW conversion (mW m^{-2}). (f) The zonal average of (e) in black; average over only positive values in red; average over only negative values in blue. Labels A through D refer to specific points of interest described in the text.

gradients (frontogenesis), and a negative value indicates weakening (frontolysis).

Figure 5d displays the mean frontogenesis function at the surface, averaged over the 4-day analysis period (wave frontogenesis is negligible here). The region along and to the south of the main zonal current exhibits intense surface frontogenesis. As anticipated, the largest magnitude mean-to-wave fluxes (Fig. 5e) occur near regions of intense frontogenesis. The mean-to-wave energy flux shown in Fig. 5e is the net surface layer energy conversion integrated over depths $z > -50$ m and averaged in time (over the 4-day analysis period). The energy fluxes into the wave field are largely localized to sharp fronts undergoing frontogenesis, consistent with the theory of spontaneous generation. There are also regions of significant energy loss from the wave field (negative mean to wave), both adjacent to regions of energy gain, and within eddies (labeled C and D). The maximum mean-to-wave energy conversion is 87 mW m^{-2} associated with the front labeled A, and there are a number of other fronts with energy conversions around 10 mW m^{-2} (e.g., the front labeled B). For comparison, the average energy flux into waves (from all sources) over the entire ocean is about 3 mW m^{-2} [based on the figure of 1.2-TW global generation suggested by Wunsch and Ferrari (2004), among others], so 10 mW m^{-2} is locally significant. However, the localized nature of the energy fluxes means that spatially averaged values are significantly less than these figures. The maximum zonally averaged value (Fig. 5f) is 0.15 mW m^{-2}, and the zonally and meridionally averaged value is just 0.02 mW m^{-2}. The vast majority (>80%) of the energy transfer to the wave field occurs through the potential mean-to-wave term, indicating that the wave energy is drawn from the APE of the mean density fronts.

b. Thermocline layer

Figure 6 displays an analogous plot to Fig. 5, but for the thermocline layer with snapshots taken at 110-m depth. In this region the flow is more balanced with the vorticity Rossby number (Fig. 6a) generally less than 0.2 and weak mean frontogenesis (Fig. 6d). The exceptions are two locations (labeled A and B) along the main zonal current where the Rossby number is large (0.8) and there is significant frontogenesis, suggesting spontaneous generation is occurring. The mean-to-wave

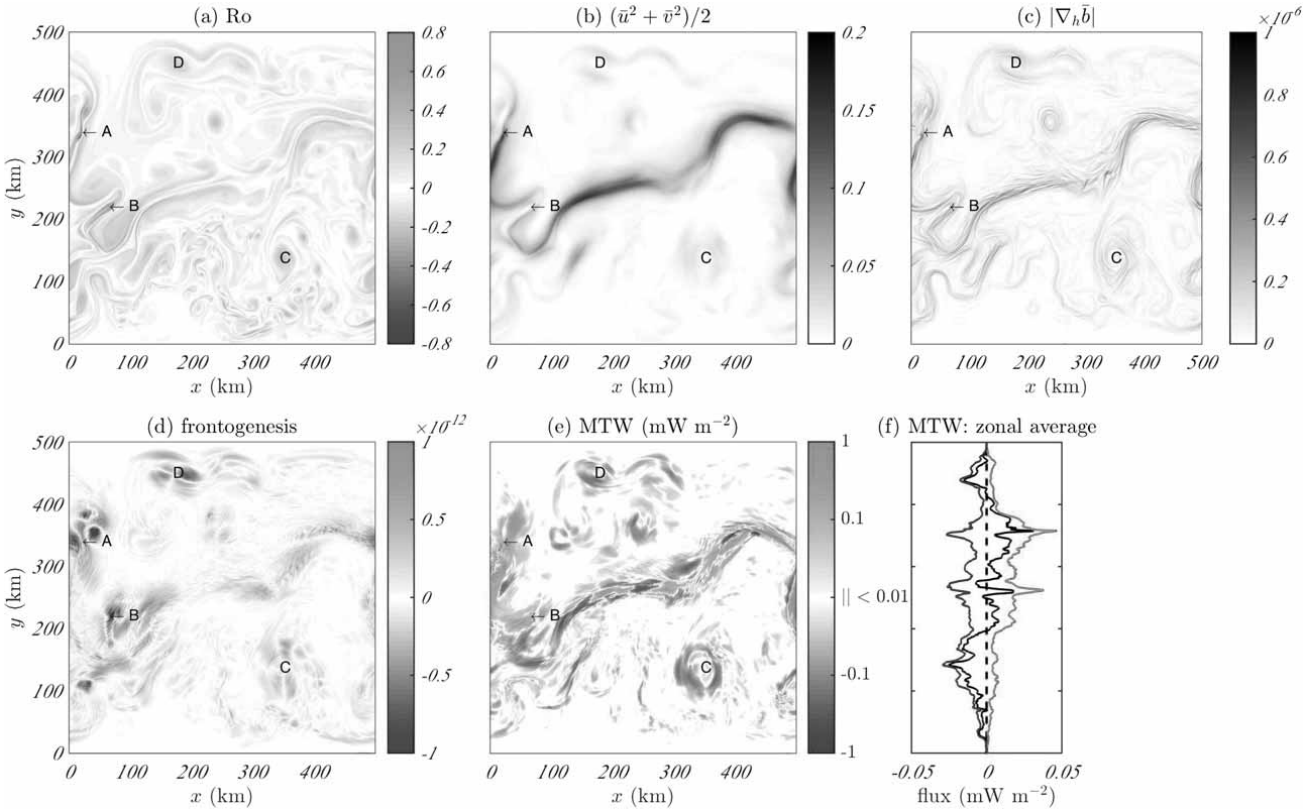

FIG. 6. As in Fig. 5, but for the thermocline layer ($z = -110$ m).

energy conversion (Fig. 6e) near these two locations is the dominant energy input into the wave field in the thermocline layer, exceeding 0.1 mW m^{-2} over a significant area. While there are large mean-to-wave flux magnitudes along the remainder of the main zonal current, they are mostly compensated with regions of large positive fluxes adjoining regions of large negative fluxes, and thus there is minimal net conversion. The sharp fronts and filaments, submesoscale eddy field, and associated positive mean-to-wave fluxes that existed in the surface layer to the south of the current are not present in the thermocline layer. Instead this region is dominated by a loss of wave energy back to the mean flow, most notably within the anticyclonic eddy labeled C. Similar behavior is observed for the cyclonic eddy labeled D to the north of the main zonal current. Both of these eddies also tended to remove wave energy in the surface layer (e.g., Fig. 5e, labels C/D), but their effect is more pronounced in the thermocline layer. The combination of apparent spontaneous generation near locations A/B, and energy loss near C/D, results in negligible net mean-to-wave energy flux in the thermocline region: $\langle \text{MTW} \rangle = -6 \times 10^{-4}$ mW m^{-2}.

c. Interior layer

Figure 7 displays a plot similar to Figs. 5 and 6 but for the interior layer with snapshots at 1000-m depth. The flow in this layer is essentially balanced with the Rossby number less than 0.1 everywhere (Fig. 7a). Frontogenesis due to the mean flow is entirely negligible and is not shown. The small Rossby numbers and negligible frontogenesis imply that there is no direct spontaneous generation in the interior layer, but despite this, there is a significant transfer of energy from the mean flow to the surface-generated wave field over a broad area (Fig. 7e). The time-averaged, depth-integrated, mean-to-wave energy flux is 0.1–0.8 mW m^{-2} in the region within the main zonal current (Fig. 7b). The energy flux is associated almost entirely with the mean-to-wave potential term (e.g., see Fig. 4) and therefore horizontal buoyancy gradients. The mean flow buoyancy gradient (Fig. 7c) shows the existence of a network of interlaced buoyancy fronts and filaments within the main current, with the strongest gradients collocated with the largest mean-to-wave conversions. The fronts have typical widths of 5 km or smaller, leading to a spatial correlation with similar scale components of the internal wave field (and in particular the horizontal wave buoyancy flux $\tilde{\mathbf{u}}_h \tilde{b}$). Despite the small width of the fronts they are essentially geostrophic (Ro < 0.1), since the cross-frontal buoyancy difference is small. The positive mean-to-wave conversion implies that the wave field is drawing energy from the available potential energy of the fronts/filaments and destroying the fronts in

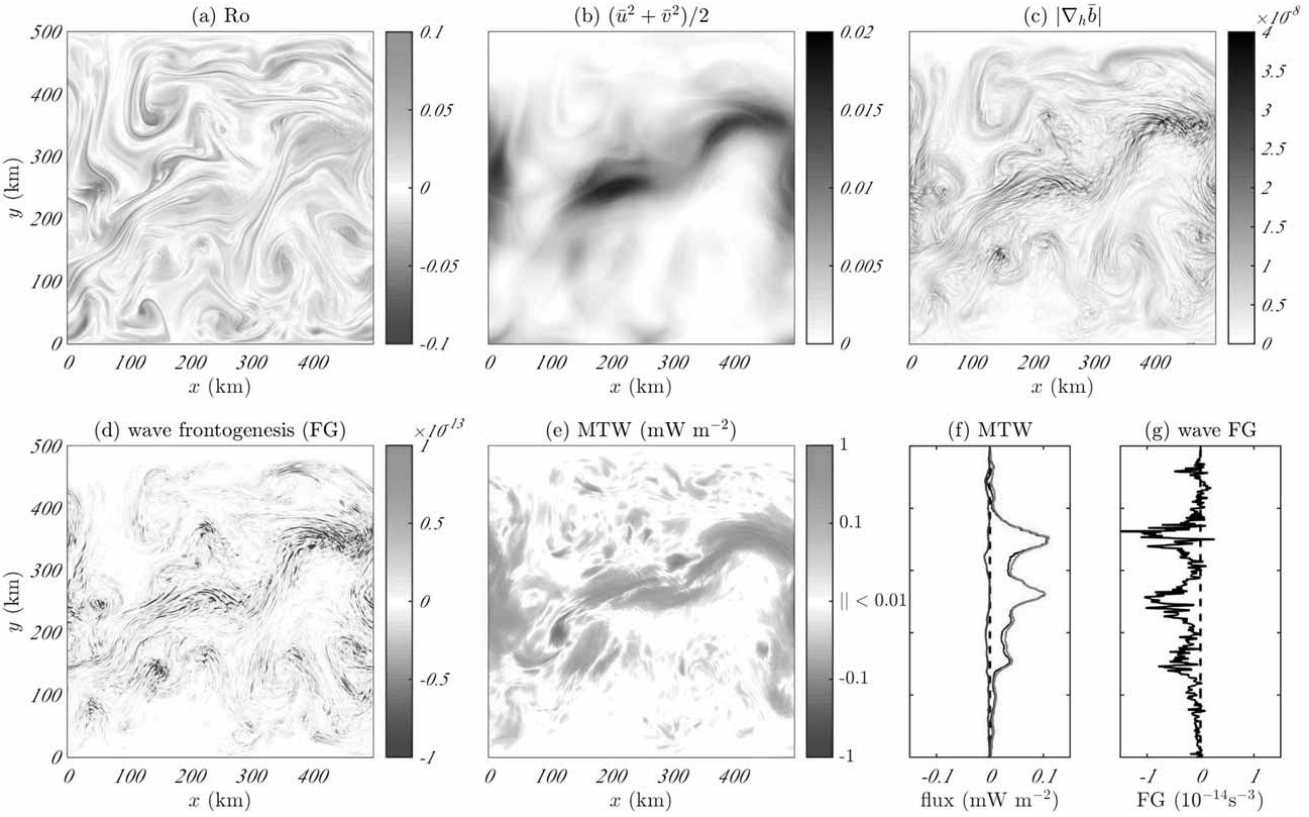

FIG. 7. As in Fig. 5, but for the interior layer ($z = -1000$ m). Additionally, (g) the zonal average of (d).

the process. Indeed, the mean-to-wave conversion is the largest sink of mean energy in the model interior, as discussed in the next section.

The effect of the wave field on the density fronts may be observed via the wave component of the frontogenesis function [Eq. (8)], a snapshot of which is plotted in Fig. 7d.[3] The snapshot shows intense frontolysis coincident with the sharp mean buoyancy gradients seen in Fig. 7c. The zonally averaged frontogenesis profile is shown in Fig. 7g and closely matches that of the zonally averaged mean-to-wave energy flux shown in Fig. 7f. The wave-forced frontolysis is dominated by the strain component $-[(\partial_x \bar{b})^2 \partial_x \tilde{u} + (\partial_y \bar{b})^2 \partial_y \tilde{v}]/|\nabla_h \bar{b}|$, indicating that the wave field is (on average) "stretching out" the sharp buoyancy filaments as the waves pass through the interior layer.

d. Mean energy sinks

The sign-definite sinks of mean energy in the model interior are the viscous dissipation of mean kinetic energy and the irreversible mixing of mean density gradients and are shown in Fig. 8a. The net mean-to-wave conversion and the potential MTW component are also shown.[4] Between 500- and 2400-m depth, the loss of mean available potential energy into waves exceeds viscous dissipation and explicit irreversible mixing by an order of magnitude. As discussed in the previous section, this loss of mean energy is associated with the destruction of interior fronts and filaments and thus the waves are acting as an effective horizontal diffusion with respect to the mean flow. The effective wave horizontal diffusivity κ_h^{wave} can be estimated by treating the MTW available potential energy sink as an "effective irreversible mixing" (e.g., Polzin 2010):

$$\text{MTW}_{\text{pot}} \equiv \frac{\kappa_h^{\text{wave}}}{N^2}|\nabla_h \bar{b}|^2 \quad \Rightarrow \quad \kappa_h^{\text{wave}} = \frac{N^2 \langle \text{MTW}_{\text{pot}} \rangle}{\langle |\nabla_h \bar{b}|^2 \rangle}. \tag{9}$$

The value of wave diffusivity computed via this method is shown in Fig. 8b as a function of depth. The wave diffusivity peaks at over 5 m^2 s^{-1} between 1200- and

[3] Only the wave-forced frontogenesis due to the horizontal velocity is shown in Fig. 7d; the vertical part is locally large in the snapshot but negligible in a time and space average. The magnitude of wave-forced frontogenesis significantly exceeds the mean-forced frontogenesis in the interior layer.

[4] The negative of MTW is shown in Fig. 8 such that a negative value represents a sink of mean energy, consistent with the mean flow dissipation and mixing terms.

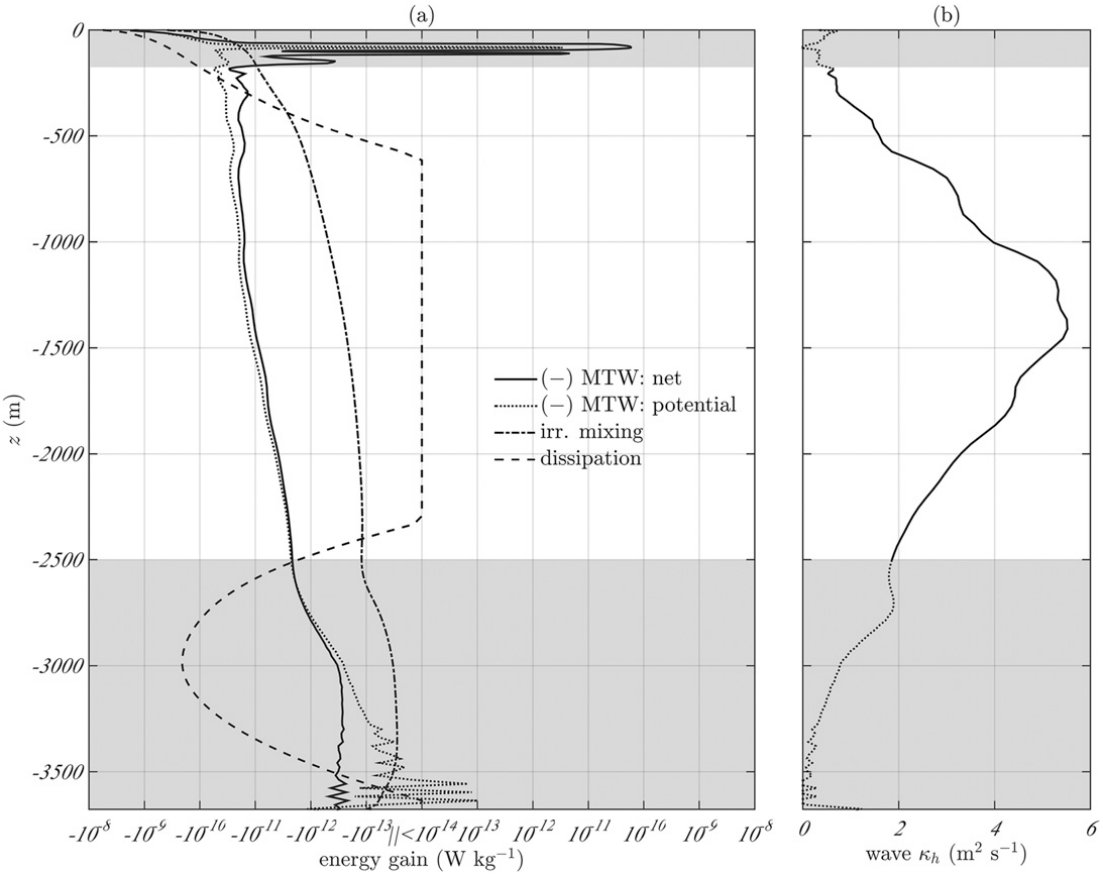

FIG. 8. Mean flow energetics. (a) Sinks of mean energy as a function of depth. The dominant sink in the interior is the loss of energy to the wave field (MTW conversion). The double-sided log scale only displays amplitudes exceeding $10^{-14}\,\mathrm{W\,kg^{-1}}$. (b) The effective wave diffusivity κ_h^{wave} as defined by Eq. (9). Regions outside the ''interior layer'' are shaded. The depth-averaged wave diffusivity in the interior layer is $3.3\,\mathrm{m^2\,s^{-1}}$.

1400-m depth and has a depth-averaged value in the interior layer of $3.3\,\mathrm{m^2\,s^{-1}}$, an order of magnitude larger than the explicit horizontal diffusivity in the model ($\kappa_h = 0.1\,\mathrm{m^2\,s^{-1}}$).

e. Summary

Figure 9 displays the vertically integrated wave energy budget for the numerical model as a bar chart. Each row shows the net contribution of a given term in the energy budget in milliwatts per square meter as the length of the bar, with colors indicating the contribution from each of the four source/sink layers identified previously: surface (cyan), thermocline (red), interior (green), and sponge (gray). The top row shows the total source and sink in each layer, and the overall flux residual is shown in black. This residual is negligible; that is, the energy budget is effectively closed.

Over the whole domain there is a net mean-to-wave conversion of $0.05\,\mathrm{mW\,m^{-2}}$, which is lost predominantly via irreversible mixing (near the surface) and viscous dissipation (in the sponge layer). The total mean-to-wave conversion—or spontaneous generation—in the surface layer is $0.021\,\mathrm{mW\,m^{-2}}$, although 73% of this is lost locally within the surface layer via irreversible mixing and dissipation. Of the remaining wave energy flux at 50-m depth, a further 74% is lost in the thermocline layer, mostly through viscous dissipation. However, in the interior layer, below 175 m, there is a strong amplification of the wave energy flux, with a total mean-to-wave conversion of $0.026\,\mathrm{mW\,m^{-2}}$. This wave energy flux is lost in the sponge layer below 2500 m, mostly through viscous dissipation, but with nonnegligible contributions from bottom drag and irreversible mixing.

4. Discussion

The most significant feature of the numerical simulations presented here is the broad-scale interior energization of the surface-generated internal waves. Between 175- and 2500-m depth, we observe an order

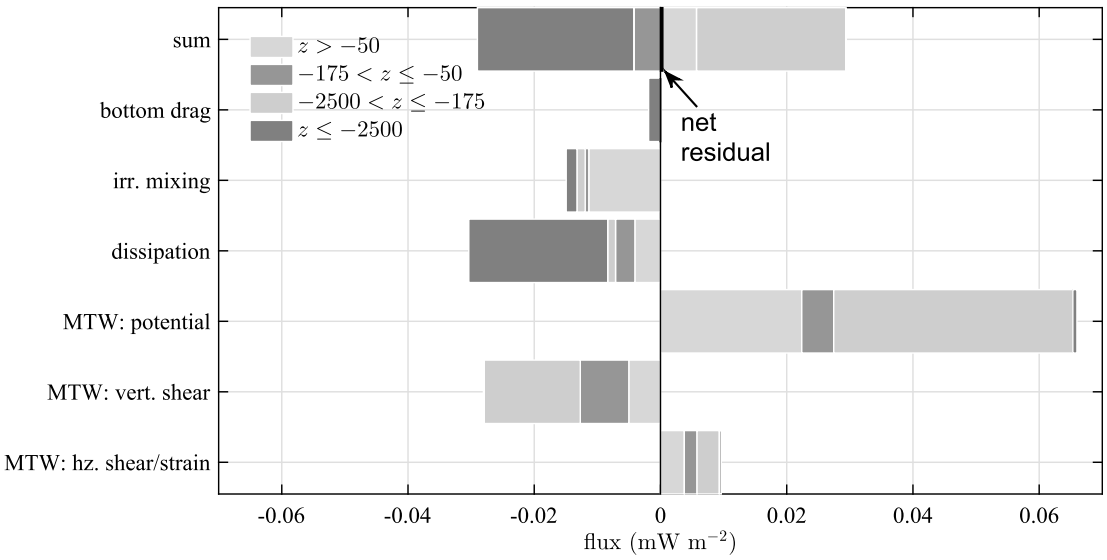

FIG. 9. The wave energy budget for the numerical model per unit area, averaged over the entire domain. The terms in the budget are defined by Eqs. (4)–(7). The individual contribution from each of the four source and sink layers identified in the text are indicated by the colors (see legend). The total source/sink in each layer is shown in the top ''sum'' bar; these sources and sinks balance to give a negligible total residual (black bar).

of magnitude increase in the net downward wave energy flux. The depth-integrated, mean-to-wave conversion in this region averages $0.03\,\mathrm{mW\,m^{-2}}$ over the entire domain, exceeding the initial surface generation of $0.02\,\mathrm{mW\,m^{-2}}$, and is therefore the dominant source of wave energy in our model. The mean-to-wave conversion is associated with waves drawing energy from narrow (but geostrophic) fronts and filaments within the large-scale zonal current with fluxes of $O(0.1\text{–}1)\,\mathrm{mW\,m^{-2}}$ throughout this region (e.g., Fig. 7e). For a steady state to be maintained, these density filaments must be continually created in (or advected into) the model interior. This process is still under investigation and will be described in a future work.

In addition to amplifying the wave field, the mean-to-wave conversion is the dominant sink of mean energy in the interior of the model ocean, exceeding both the explicit viscous dissipation and irreversible mixing. The destruction of interior buoyancy gradients by the waves can be treated as an effective irreversible mixing in respect to the mean flow (e.g., Polzin 2010) with an average ''wave horizontal diffusivity'' of $3.3\,\mathrm{m^2\,s^{-1}}$, an order of magnitude larger than the explicit horizontal diffusivity used in the model ($0.1\,\mathrm{m^2\,s^{-1}}$). These results suggest that the interior amplification of waves seen in the present simulation is unlikely to be significant in models with $O(1)\,\mathrm{m^2\,s^{-1}}$ or larger explicit horizontal diffusivity (e.g., Nagai et al. 2015), since the explicit diffusivity would tend to destroy the frontal structures and thereby reduce the potential energy source for the wave field. Thus, as argued by Shakespeare and Hogg (2017), the use of smaller turbulent diffusive parameters in modeling allows a greater range of possible internal wave dynamics.

The concept of significant mean-to-wave energy fluxes in the ocean interior is not unprecedented. Analysis of observations from moorings in the Gulf Stream recirculation at 800-m depth yield mean-to-wave conversion estimates of $4 \times 10^{-10}\,\mathrm{W\,kg^{-1}}$ (Polzin 2010, and references therein). Polzin (2010) concludes that this mean-to-wave conversion is the dominant source of wave energy in the Gulf Stream recirculation. If the observed energy flux density ($4 \times 10^{-10}\,\mathrm{W\,kg^{-1}}$) is constant over 2000 m of ocean depth, it equates to a net mean-to-wave flux of approximately $0.8\,\mathrm{mW\,m^{-2}}$, comparable to the fluxes observed within the main zonal current in the present simulation (Fig. 7e).

The model used here has been carefully configured such that internal wave generation can only occur ''spontaneously'' from unbalanced flow near the ocean surface. This spontaneous generation is highly localized in space, predominantly near strong fronts and filaments in the upper 50 m. The time-mean energy flux into waves is typically $O(1\text{–}10)\,\mathrm{mW\,m^{-2}}$ at fronts undergoing intense frontogenesis but can be as high as $87\,\mathrm{mW\,m^{-2}}$ (Fig. 5e). The peak magnitudes of these energy fluxes are comparable to those associated with lee-wave generation at topography (Bell 1975; Nikurashin et al. 2014), suggesting spontaneous generation may be locally significant in the ocean. The $O(10)\,\mathrm{mW\,m^{-2}}$ fluxes are also comparable to those

seen by Nagai et al. (2015) in their model of spontaneous generation in the Kuroshio.

However, the localized nature of the spontaneous generation means that the spatially averaged energy fluxes in the present simulation are significantly smaller than the local values. The zonally (along channel) averaged values peak at $0.15\,\mathrm{mW\,m^{-2}}$, and the net layer-integrated flux down to 50-m depth is just $0.02\,\mathrm{mW\,m^{-2}}$. Nagai et al. (2015) take the approach of averaging the positive and negative mean-to-wave fluxes separately; from this perspective, the net surface input to the wave field is $0.074\,\mathrm{mW\,m^{-2}}$, with $0.053\,\mathrm{mW\,m^{-2}}$ (73%) lost back to the mean flow within the surface layer, similar to the 85% reported by Nagai et al. (2015). However, in our model the majority of the mean-to-wave flux occurs through the potential term [see Eq. (7)] rather than the strain term (as in their model), suggesting that the mechanism of spontaneous generation may be different.

A number of caveats apply to our results. First, our model exhibits significant near-surface wave energy loss through the irreversible mixing and dissipation of the spontaneously generated waves. Between the surface and 175-m depth, over 90% of the net spontaneously generated wave energy is lost through these processes. It is likely that a significant fraction of this energy loss is a direct result of the artificially large values of horizontal viscosity ($3\,\mathrm{m^2\,s^{-1}}$ near the surface) and diffusivity ($0.1\,\mathrm{m^2\,s^{-1}}$) required for model stability and thus is essentially spurious (Shakespeare and Hogg 2017). With smaller viscous and diffusive parameters (e.g., at higher resolution), we anticipate that the wave energy flux passing through 175-m depth could be significantly larger, potentially resulting in an enhanced mean-to-wave conversion in the model interior.

Second, the extent to which the magnitude of spontaneous generation could change in the presence of a more energetic eddy field (e.g., because of the wind forcing, which is not present in our simulations) or at higher resolution (i.e., permitting smaller turbulent parameters and sharper fronts) remains uncertain. Theoretical models of spontaneous generation (e.g., Shakespeare and Taylor 2014) predict exponentially larger wave generation for a linear increase in the strength of the eddy field and associated strain. Theory also predicts that spontaneous generation is further amplified at sharper fronts. Thus, it is possible that some of the energy that is currently dissipated from the mean flow (e.g., Fig. 8) as frontal scales approach the model resolution could be redirected into the wave field at higher resolution.

Third, we have used the highly idealized configuration of a flat-bottomed ocean basin with no surface forcing and a sponge in the deep ocean to absorb downward-propagating waves. In this configuration, there is a single source of waves at the ocean surface; these waves propagate downward and are amplified by the mean flow before finally dissipating in the bottom sponge. The net wave energy flux is thus downward (on average) everywhere in the domain, something that would not necessarily be true in a more realistic model that permits reflections off the bottom and/or bottom wave generation at topography. Initial results from such model configurations suggest that the strength and directionality of the wave energy flux can be a crucial factor in controlling the interior mean-to-wave conversion seen in the present model. These effects will be studied in detail in a future work.

5. Conclusions

There are two major implications of our modeling study for the ocean's energy budget. First, our model indicates a potential role for spontaneous generation as a notable energy source in strongly eddying regions of the ocean. As noted above, further studies are required to better constrain the magnitude of spontaneous generation in comparison to other wave sources. Second, our results suggest that the ocean interior has the potential to be a significant source of wave energy and a sink of nonwave energy. Thus, the current paradigm of surface- or bottom-generated internal waves transporting energy into the ocean interior may be inverted in some circumstances to one where internal waves transfer energy to the boundary where turbulence and mixing is commonplace.

Acknowledgments. Both authors acknowledge funding from the ARC Centre of Excellence for Climate System Science Grant Number CE1101028.

APPENDIX

Wave Energy Budget

Here, we derive a generic wave energy budget for a hydrostatic numerical model. Unlike previous wave energy equations (Muller 1976) we make no assumption as to the quasigeostrophy of the nonwave flow. To begin, consider filtering a given field into two parts: a wave part $\tilde{u}$ and a nonwave part $\overline{u}$, where $u = \overline{u} + \tilde{u}$. At this point we make no assumptions about the form of this filtering. For a hydrostatic flow, the wave kinetic energy is

$$\tilde{k} = \frac{1}{2}(\tilde{u}^2 + \tilde{v}^2), \tag{A1}$$

and the wave APE is defined as

$$\tilde{a} = \frac{\tilde{b}^2}{2N^2}, \tag{A2}$$

where $N^2(z) = \partial_z \langle \overline{b} \rangle$ is the mean stratification at depth z. To form the wave kinetic energy equation we take the dot product of the horizontal momentum equations with the horizontal wave velocity:

$$\tilde{\mathbf{u}}_h \cdot \left(\frac{\partial \mathbf{u}_h}{\partial t} + \mathbf{u} \cdot \nabla \mathbf{u}_h + f\hat{\mathbf{z}} \times \mathbf{u}_h = -\frac{1}{\rho_0} \nabla_h p + \nabla \cdot A_h \nabla \mathbf{u}_h + \frac{\partial}{\partial z} A_v \frac{\partial}{\partial z} \mathbf{u}_h \right). \tag{A3}$$

Expanding fields into their wave and nonwave parts and rewriting Eq. (A3) in terms of the wave kinetic energy (and applying hydrostatic balance) yields

$$\frac{\partial \tilde{k}}{\partial t} + \nabla \cdot (\mathbf{u}\tilde{k}) = p \nabla \cdot \tilde{\mathbf{u}} + \tilde{w} b - \frac{1}{\rho_0} \nabla \cdot (\tilde{\mathbf{u}} p) - \tilde{\mathbf{u}}_h \cdot (\mathbf{u} \cdot \nabla) \overline{\mathbf{u}}_h - \frac{\partial \overline{\mathbf{u}}_h}{\partial t} \cdot \tilde{\mathbf{u}}_h - A_h \nabla \tilde{\mathbf{u}}_h \cdot \nabla \mathbf{u}_h + \nabla_h \cdot A_h (\nabla_h \tilde{k} + \tilde{\mathbf{u}}_h \cdot \nabla_h \overline{\mathbf{u}}_h) - A_v \left(\frac{\partial \tilde{\mathbf{u}}_h}{\partial z} \cdot \frac{\partial \mathbf{u}_h}{\partial z} \right) + \frac{\partial}{\partial z} A_v \left(\frac{\partial \tilde{k}}{\partial z} + \tilde{\mathbf{u}}_h \cdot \frac{\partial \overline{\mathbf{u}}_h}{\partial z} \right). \tag{A4}$$

Note that a term involving the divergence of the wave flow $\nabla \cdot \tilde{\mathbf{u}}$ has been retained in Eq. (A4), since for an arbitrary filter there is no guarantee that the divergence is zero. To form the APE equation, we multiply the buoyancy equation by $\tilde{b}/N^2$ or

$$\frac{\tilde{b}}{N^2} \left[\frac{\partial b}{\partial t} + \mathbf{u} \cdot \nabla b = \nabla \cdot \kappa_h \nabla b + \frac{\partial}{\partial z} \kappa_v \frac{\partial b}{\partial z} - \frac{b - B_0(x,y,z)}{\tau} M(y) \right]. \tag{A5}$$

The term due to the buoyancy-restoring sponge near the northern and southern boundaries has been included in Eq. (A5): $B_0(x, y, z)$ represents the restoring profiles (i.e., Fig. 1b);$M(y)$ represents the longitudinal mask, which varies smoothly from one at the boundaries to zero in the interior; and τ represents the relaxation time scale (10 days). Expanding fields into their wave and nonwave parts and rewriting Eq. (A5) in terms of the wave APE yields

$$\frac{\partial \tilde{a}}{\partial t} + \nabla \cdot (\mathbf{u}\tilde{a}) = -w\tilde{b} \frac{\partial_z \overline{b}}{N^2} + \frac{1}{2} w \tilde{b}^2 \partial_z N^{-2} - \frac{\partial \overline{b}}{\partial t} \frac{\tilde{b}}{N^2} - \tilde{b} \tilde{\mathbf{u}}_h \cdot \frac{\nabla_h \overline{b}}{N^2} - \frac{\kappa_h}{N^2} \nabla_h \tilde{b} \cdot \nabla_h b + \nabla_h \cdot \kappa_h \left(\nabla_h \tilde{a} + \frac{\tilde{b}}{N^2} \nabla_h \overline{b} \right) - \frac{\kappa_v}{N^2} \left(\frac{\partial \tilde{b}}{\partial z} \frac{\partial b}{\partial z} \right) + \frac{1}{N^2} \frac{\partial}{\partial z} \left(\tilde{b} \kappa_v \frac{\partial b}{\partial z} \right) - \frac{\tilde{b}^2 M}{N^2 \tau} - \frac{\tilde{b}(\overline{b} - B_0) M}{N^2 \tau}. \tag{A6}$$

No assumptions as to the definition of wave and nonwave fields have been made to this point.

To proceed further we introduce the assumption that there exists a temporal–spatial scale separation between the wave and nonwave fields (to be justified from the model in question) such that the temporal–spatial average of the product of a wave field $\tilde{\eta}$ and nonwave field $\overline{\theta}$ is zero, $\langle \tilde{\eta} \overline{\theta} \rangle = 0$, with the angled brackets defined by Eq. (1). We further assume that $\langle \tilde{\eta} \overline{\theta}\, \overline{\alpha} \rangle = 0$, where $\overline{\alpha}$ is another nonwave field. These assumptions are expected be valid for any sensibly defined wave field, such as via a Lagrangian filter. With these assumptions the wave kinetic energy equation [Eq. (A4)], assuming a steady wave field, flat bottom, and free-slip vertical sidewalls, becomes

$$\frac{\partial}{\partial z} \langle w\tilde{k} \rangle = \langle \tilde{w}\tilde{b} \rangle - \frac{1}{\rho_0} \frac{\partial}{\partial z} \langle \tilde{w}\tilde{p} \rangle + \langle -\tilde{\mathbf{u}}_h \cdot (\tilde{\mathbf{u}} \cdot \nabla) \overline{\mathbf{u}}_h \rangle - \left\langle A_h |\nabla_h \tilde{\mathbf{u}}_h|^2 + A_v \left| \frac{\partial \tilde{\mathbf{u}}_h}{\partial z} \right|^2 \right\rangle + \frac{\partial}{\partial z} \left\langle A_v \frac{\partial \tilde{k}}{\partial z} \right\rangle + \langle \tilde{p} \cancel{\nabla \cdot \tilde{\mathbf{u}}} \rangle. \tag{A7}$$

The divergence term in Eq. (A7) may now be neglected since the continuity equation implies that $\nabla \cdot \tilde{\mathbf{u}} = -\nabla \cdot \overline{\mathbf{u}}$ and thus $\langle \tilde{p} \nabla \cdot \tilde{\mathbf{u}} \rangle = \langle -\tilde{p} \nabla \cdot \overline{\mathbf{u}} \rangle$, which is zero by assumption. The wave APE equation [Eq. (A6)], with the same assumptions, becomes

$$\frac{\partial}{\partial z}\langle w\tilde{a}\rangle = -\left\langle \tilde{w}\tilde{b}\frac{\partial_z \overline{b}}{N^2}\right\rangle + \left\langle \frac{1}{2}w\tilde{b}^2\partial_z N^{-2}\right\rangle + \left\langle -\tilde{b}\tilde{\mathbf{u}}_h\cdot\frac{\nabla_h \overline{b}}{N^2}\right\rangle - \left\langle \frac{\kappa_h}{N^2}|\nabla_h\tilde{b}|^2 + \frac{\kappa_v}{N^2}\left(\frac{\partial\tilde{b}}{\partial z}\right)^2\right\rangle + \left\langle \frac{1}{N^2}\frac{\partial}{\partial z}\left(\tilde{b}\kappa_v\frac{\partial\tilde{b}}{\partial z}\right)\right\rangle - \left\langle\frac{2\tilde{a}M}{\tau}\right\rangle. \tag{A8}$$

We now sum the space–time-averaged kinetic energy [Eq. (A7)] and available potential energy [Eq. (A8)] equations to obtain an equation for total wave energy $\tilde{e} = \tilde{k} + \tilde{a}$:

$$\frac{1}{\rho_0}\frac{\partial}{\partial z}\langle\tilde{w}\tilde{p}\rangle = -\frac{\partial}{\partial z}\langle w\tilde{e}\rangle + \left\langle \tilde{w}\tilde{b}\left(1-\frac{\partial_z\overline{b}}{N^2}\right)\right\rangle + \left\langle\frac{1}{2}w\tilde{b}^2\partial_z N^{-2}\right\rangle + \langle -\tilde{\mathbf{u}}_h\cdot(\tilde{\mathbf{u}}\cdot\nabla)\overline{\mathbf{u}}_h\rangle$$
$$+ \left\langle -\tilde{b}\tilde{\mathbf{u}}_h\cdot\frac{\nabla_h\overline{b}}{N^2}\right\rangle - \tilde{\varepsilon} - \tilde{\phi}_i - \tilde{\phi}_{\text{sponge}} + \frac{\partial}{\partial z}\left\langle A_v\frac{\partial\tilde{k}}{\partial z}\right\rangle + \left\langle\frac{1}{N^2}\frac{\partial}{\partial z}\left(\tilde{b}\kappa_v\frac{\partial\tilde{b}}{\partial z}\right)\right\rangle, \tag{A9}$$

where ε is the viscous dissipation by waves [Eq. (4)], ϕ_i is the irreversible mixing by waves [Eq. (5)], and $\tilde{\phi}_{\text{sponge}} = \langle(2\tilde{a}M)/\tau\rangle$ is the (sign definite) damping of waves by the buoyancy-restoring sponge. If we define the vertical stress as

$$\tilde{\boldsymbol{\tau}}_h = A_v\frac{\partial\tilde{\mathbf{u}}_h}{\partial z}, \tag{A10}$$

and assume there are no surface buoyancy fluxes or wind stresses, the vertically integrated wave energy budget is

$$0 = -\int_{\text{bot}}\tilde{\mathbf{u}}_h\cdot\tilde{\boldsymbol{\tau}}_h\,dS - \int\tilde{\varepsilon}\,dz - \int\tilde{\phi}_i\,dz - \int\tilde{\phi}_{\text{sponge}}\,dz + \int\left(\langle-\tilde{\mathbf{u}}_h\cdot(\tilde{\mathbf{u}}\cdot\nabla)\overline{\mathbf{u}}_h\rangle + \left\langle-\tilde{b}\tilde{\mathbf{u}}_h\cdot\frac{\nabla_h\overline{b}}{N^2}\right\rangle\right)dz$$
$$+ \int\left(\left\langle\tilde{w}\tilde{b}\left(1-\frac{\partial_z\overline{b}}{N^2}\right)\right\rangle + \left\langle\frac{1}{2}w\tilde{b}^2\partial_z N^{-2}\right\rangle - \left\langle\kappa_v\tilde{b}\frac{\partial\tilde{b}}{\partial z}\partial_z N^{-2}\right\rangle\right)dz. \tag{A11}$$

The top line in Eq. (A11) is composed of the sign-definite energy sinks; in order, these are bottom drag, viscous dissipation, irreversible mixing, and damping from the buoyancy-restoring sponge. The damping term is negligible for the long restoring time scale (10 days) and small spatial extent of the sponge used in the present simulations. The second line is composed of the dominant mean-to-wave conversion terms from the kinetic (left-hand term) and potential (right hand) energy equations. The kinetic mean-to-wave term is expanded in the main text [Eq. (7)] into horizontal shear and strain and vertical shear terms. As noted in the main text, these mean-to-wave terms differ from previous energy budgets (Muller 1976; Polzin 2010) in that the time averaging (included in the definition of the angled bracket) is done after the multiplication of the mean and wave components. The bottom line in Eq. (A11) is composed of the remaining mean-to-wave terms, which all involve correlations of wave fields with spatial variations of the stratification. These terms are each individually negligible in the present model.

REFERENCES

Bell, T., 1975: Topographically generated internal waves in the open ocean. *J. Geophys. Res.*, **80**, 320–327, doi:10.1029/JC080i003p00320.

Blumen, W., 1972: Geostrophic adjustment. *Rev. Geophys. Space Phys.*, **10**, 485–528, doi:10.1029/RG010i002p00485.

Booker, J. R., and F. P. Bretherton, 1967: The critical layer for internal gravity waves in a shear flow. *J. Fluid Mech.*, **27**, 513–539, doi:10.1017/S0022112067000515.

Danioux, E., J. Vanneste, P. Klein, and H. Sasaki, 2012: Spontaneous inertia-gravity-wave generation by surface-intensified turbulence. *J. Fluid Mech.*, **699**, 153–173, doi:10.1017/jfm.2012.90.

Grisouard, N., M. B. Fox, and J. Nijjer, 2016: Radiation of internal waves by symmetrically unstable fronts. *Eighth Int. Symp. on Stratified Flows*, San Diego, CA, University of California, San Diego, 1–8. [Available online at http://escholarship.org/uc/item/2b59h10g#page-1.]

Lott, F., R. Plougonven, and J. Vanneste, 2010: Gravity waves generated by sheared potential vorticity anomalies. *J. Atmos. Sci.*, **67**, 157–170, doi:10.1175/2009JAS3134.1.

Marshall, J., A. Adcroft, C. Hill, L. Perelman, and C. Heisey, 1997: A finite-volume, incompressible Navier Stokes model for studies of the ocean on parallel computers. *J. Geophys. Res.*, **102**, 5753–5766, doi:10.1029/96JC02775.

Miller, J. E., 1948: On the concept of frontogenesis. *J. Meteor.*, **5**, 169–171, doi:10.1175/1520-0469(1948)005<0169:OTCOF>2.0.CO;2.

Muller, P., 1976: On the diffusion of momentum and mass by internal gravity waves. *J. Fluid Mech.*, **77**, 789–823, doi:10.1017/S0022112076002899.

Munk, W., 1981: Internal waves and small-scale processes. *Evolution of Physical Oceanography*, B. A. Warren and C. Wunsch, Eds., MIT Press, 264–291.

Nagai, T., A. Tandon, E. Kunze, and A. Mahadevan, 2015: Spontaneous generation of near-inertial waves by the Kuroshio Front. *J. Phys. Oceanogr.*, **45**, 2381–2406, doi:10.1175/JPO-D-14-0086.1.

Nikurashin, M., and R. Ferrari, 2011: Global energy conversion rate from geostrophic flows into internal lee waves in the deep ocean. *Geophys. Res. Lett.*, **38**, L08610, doi:10.1029/2011GL046576.

——, ——, N. Grisouard, and K. Polzin, 2014: The impact of finite-amplitude bottom topography on internal wave generation in the Southern Ocean. *J. Phys. Oceanogr.*, **44**, 2938–2950, doi:10.1175/JPO-D-13-0201.1.

Plougonven, R., and V. Zeitlin, 2009: Nonlinear development of inertial instability in a barotropic shear. *Phys. Fluids*, **21**, 106601, doi:10.1063/1.3242283.

Polzin, K. L., 2010: Mesoscale eddy–internal wave coupling. Part II: Energetics and results from PolyMode. *J. Phys. Oceanogr.*, **40**, 789–801, doi:10.1175/2009JPO4039.1.

——, and Y. V. Lvov, 2011: Toward regional characterizations of the oceanic internal wavefield. *Rev. Geophys.*, **49**, RG4003, doi:10.1029/2010RG000329.

Ribstein, B., R. Plougonven, and V. Zeitlin, 2014: Inertial versus baroclinic instability of the Bickley jet in continuously stratified rotating fluid. *J. Fluid Mech.*, **743**, 1–31, doi:10.1017/jfm.2014.26.

Shakespeare, C. J., 2015: On the generation of waves during frontogenesis. Ph.D. thesis, University of Cambridge, 221 pp.

——, and J. R. Taylor, 2014: The spontaneous generation of inertia–gravity waves during frontogenesis forced by large strain: Theory. *J. Fluid Mech.*, **757**, 817–853, doi:10.1017/jfm.2014.514.

——, and ——, 2016: Spontaneous wave generation at strongly strained density fronts. *J. Phys. Oceanogr.*, **46**, 2063–2081, doi:10.1175/JPO-D-15-0043.1.

——, and A. M. Hogg, 2017: The viscous lee wave problem and its implications for ocean modelling. *Ocean Modell.*, **113**, 22–29, doi:10.1016/j.ocemod.2017.03.006.

Thomas, L. N., 2012: On the effects of frontogenetic strain on symmetric instability and inertia–gravity waves. *J. Fluid Mech.*, **711**, 620–640, doi:10.1017/jfm.2012.416.

Whitt, D. B., and L. N. Thomas, 2015: Resonant generation and energetics of wind-forced near-inertial motions in a geostrophic flow. *J. Phys. Oceanogr.*, **45**, 181–208, doi:10.1175/JPO-D-14-0168.1.

Winters, K. B., P. N. Lombard, J. J. Riley, and E. A. D'Asaro, 1995: Available potential energy and mixing in density-stratified fluids. *J. Fluid Mech.*, **289**, 115–128, doi:10.1017/S002211209500125X.

Wunsch, C., and R. Ferrari, 2004: Vertical mixing, energy and the general circulation of the oceans. *Annu. Rev. Fluid Mech.*, **36**, 281–314, doi:10.1146/annurev.fluid.36.050802.122121.